Materials Science & Engineering A 937 (2025) 148461

Contents lists available at ScienceDirect

Materials Science & Engineering A

journal homepage: www.elsevier.com/locate/msea

Tracking phase-level properties in heat-treated high-chromium cast irons using mechanical microscopy

M.A. Guitar [a,*], U.P. Nayak [a], G. Riu-Perdrix [b], J.M. Wheeler [c,**], J.J. Roa [b]

[a] Department of Materials Science, Saarland University, Campus D3.3, D-66123, Saarbrücken, Germany
[b] Steros GPA Innovative S.L., 08030, Barcelona, Spain
[c] Laboratory for Nanometallurgy, ETH Zurich, Vladimir-Prelog-Weg 5, Zurich, 8093, Switzerland

ARTICLE INFO

Keywords:
Mechanical microscopy
High-speed nanoindentation
Mechanical properties
High chromium cast irons

ABSTRACT

Determining individual microstructural components in multicomponent and multiscale materials can be a challenging task. High chromium cast irons (HCCI), particularly in heat-treated states, exhibit complex microstructures that include austenite or martensite on a meso-scale, as well as hard and micro-sized eutectic carbides, and secondary carbides on a sub-micron or nanometric length scale. Assessing the mechanical properties and quantities of these phases requires small scale characterization over relatively large areas.

In the current work, the mechanical properties of each individual constitutive phase were determined by using high-speed nanoindentation maps as a function of four different heat treatments. An area of 400 × 300 μm containing 30 000 indentations on each sample was analysed. Statistical deconvolution and machine-learning clustering methods were used to determine the hardness and elastic modulus of the different microstructural components. The results illustrate how the microstructure and mechanical properties of the various phases evolve through heat treatment, supporting the notion that secondary carbides reinforce and strength the HCCI matrix, rather than acting as an individual component.

1. Introduction

High chromium cast irons (HCCI) represent an important alloy class for mining and manufacturing applications due to their excellent erosion performance, attributable to their high hardness and corrosion resistance [1]. This arises from the high chromium content, which impedes the formation of graphite or cementite phases, instead promoting the formation of hard, eutectic carbides (EC). In the as-cast state, the microstructure of HCCI consists of interconnected rods of eutectic carbides of the M_7C_3 (M: Cr, Fe) type, embedded an austenitic matrix with a thin region of martensite at the interface of the matrix and eutectic carbides [1]. Following the heat treatment (HT), the microstructure becomes more complex. This is due to the precipitation of secondary carbides (SC) and the austenitic matrix transforming to ferrite or martensite. At this point, the microstructure of the HCCIs show a complex multi-component and multi-scale microstructure consisting of an austenitic, ferritic, or martensitic matrix on a meso-scale [2,3]; hard and micro-sized EC, and hard SC (which may or may not be of the same nature as EC) [4–7] on a sub-micron or nanometric length scale.

From a mechanical point of view, HCCIs can be considered a quasi-metallic/ceramic composite material due to the interaction between several of its constituents. In addition to the inherent complexity of tailoring the microstructure, the current challenge confronting materials of this kind stems from the need to accurately characterize each constituent phase at an individual level, given their multi-scale nature. Improvements in experimental nanomechanics have made high-speed nanoindentation mapping a powerful tool for characterizing microstructural features and mechanical properties across relatively large areas with micron-scale resolution [8]. This effectively transforms high-speed nanoindentation mapping into a *mechanical microscopy* technique. This approach allows for a detailed analysis of microstructural features and their correlation with the intrinsic mechanical properties of each constitutive phase, including hardness (H), elastic modulus (E), and the plasticity index (known as the H/E ratio) [9–14]. The plasticity index, H/E, in nano-indentation testing is a measure of the plastic fraction of the total work of indentation (W_p/W_{total}) [15] or the

This article is part of a special issue entitled: Nanomechanical Testing 2024 published in Materials Science & Engineering A.

* Corresponding author.
** Corresponding author.
E-mail addresses: a.guitar@mx.uni-saarland.de (M.A. Guitar), Jeff.Wheeler@oxinst.com (J.M. Wheeler).

https://doi.org/10.1016/j.msea.2025.148461
Received 25 February 2025; Received in revised form 29 April 2025; Accepted 5 May 2025
Available online 8 May 2025

resistance of the material to plastic deformation. This has been shown to be a strong indicator of abrasive performance [16]. This term should not be exchanged by the ability of the material to undergo plastic deformation without fracture, represented by the difference between plastic strain at fracture and elastic strain at yield (ε_f - ε_y) [xx]. Furthermore, it is necessary to highlight that the mechanical response of the HCCI is a direct consequence of its microstructure, principally of the volume fraction, size, and distribution of carbides, both the EC and the SC precipitated during the HT [17–20]. As shown in previous studies [17, 18,21], a variety of static responses were observed under sliding wear tests. Integrating these with mechanical microscopy will facilitate further advancement in the field. This will facilitate a more profound comprehension of the mechanical behavior of the 'composite' material at the micrometer scale. The knowledge gained will serve as a foundation for further refinement on the microstructure of the composite material.

Although the mechanical properties and tribological performance of HCCI have been extensively studied from a macroscopic perspective, the characterization at the small-scale is quite limited for these materials. To address this, mechanical microscopy combined with statistical analysis [8,14,22] and machine learning clustering algorithms will provide information about the content and distribution of the constitutive phases. This technique enables the mapping and local resolution of the mechanical properties, specifically *H* and *E* of heterogenous materials over a large area in a reasonable amount of time. The resolution of this technique is directly dependent on the indentation depth and spacing. The microstructure of HCCI can be complex, particularly after HT, which may pose a challenge for the massive indentation technique. Therefore, a microstructural analysis is recommended to be performed simultaneously to determine the appropriate length scale for investigation.

In this work, mechanical microscopy is employed to characterize the properties of individual phases within 26 wt% Cr HCCIs as a function of thermal processing, resulting in several combinations of martensite, retained austenite, and SC fractions. This enables the determination and analysis of the properties of the constituent phases within the microstructure. This study compares the performance of statistical and machine learning analysis for the determination of phase-level properties within HCCIs after a series of heat treatments.

2. Methodology

A HCCI alloy containing 2.53 wt% C, 26.6 wt% Cr and other minor alloy elements was used in this work. More information can be found in Ref. [23]. The alloy was manufactured in an arc furnace and cast at ~1450 °C into rectangular (Y) shaped sand molds hardened with phenolic resin. The samples were cut into pieces 20 × 20 × 10 mm using a water-based coolant abrasive disc. All the samples were taken from the same region to avoid possible microstructural or chemical variations. Four different treatments were applied, as schematically illustrated in Fig. 1. First, an As-cast sample is used as a reference. Then, a destabilization and a multi-step HT were applied to the samples. For the destabilization process, the samples were heated up to 980 °C with a heating rate of around 0.25 °C/s. The specimen was held at the maximum temperature for two sets of times; 0 and 90 min (labeled as Q_0 and Q_90, respectively) and subsequently quenched in water. The multi-step HT (sample SCD + Q), shown in blue in Fig. 1, includes a destabilization at 980 °C for 90 min (step 1) followed by a sub-critical diffusion step at 650 °C for 12 h (step 2) and quenching in water. A third step includes a second destabilization process at 980 °C for 90 min and quenching (step 3). For further details on the multi-step HT, refer to Refs. [6,7].

Prior to the microstructural and mechanical characterization, the specimens were embedded in conductive resin and subsequently chemo-mechanically polished (CMP) until reaching a mirror-like surface. More information about the CMP process for these types of specimens is described in Refs. [5,6]. The polished samples were etched with Villella's reagent (1 g picric acid + 5mLHCl + 95 mLC_2H_5OH) for general microstructure revelation [24]. The microstructure of the samples was analysed using a FEI Helios Nanolab field emission scanning electron microscope (FE-SEM) working with an acceleration voltage of 5–15 kV and a beam current of 1.4 nA. Electron backscattered diffraction (EBSD) was used to investigate the distribution of the microstructural components. The measurements were performed at an acceleration voltage of 20 kV and a beam current of 11 nA. The energy dispersive spectroscopy (EDAX) Hikari EBSD camera is equipped in the FE-SEM workstation. The EBSD data was analysed using the Orientation Imaging Microscopy (OIM™ v. 7, data analysis software by EDAX Inc). The post-processing of the EBSD dataset commenced with the implementation of standard noise reduction algorithms (grain confidence index (CI) standardization and grain dilation). This was followed by the elimination of all points showing a CI value of less than 0.1.

The phases contained in each of the samples were previously identified by X-ray diffraction (XRD) using a PANalytical Empyrean diffractometer system equipped with a Bragg Brentano-HD (BBHD) module and an ultra-fast PIXcel3D detector [5,18]. Additionally, the volume fraction of the RA was estimated by the Rietveld refinement approach [25], using the software Material Analysis Using Diffraction (MAUD) [26]. For the determination of the size and volume fraction of the SC, the samples were etched a modified Murakami's reagent [23,24] and analysed with the FE-SEM using a high sensitivity backscattered electron detector (vCD) for a better contrast between the phases. The carbide volume fraction (CVF) and the SC size were calculated after a

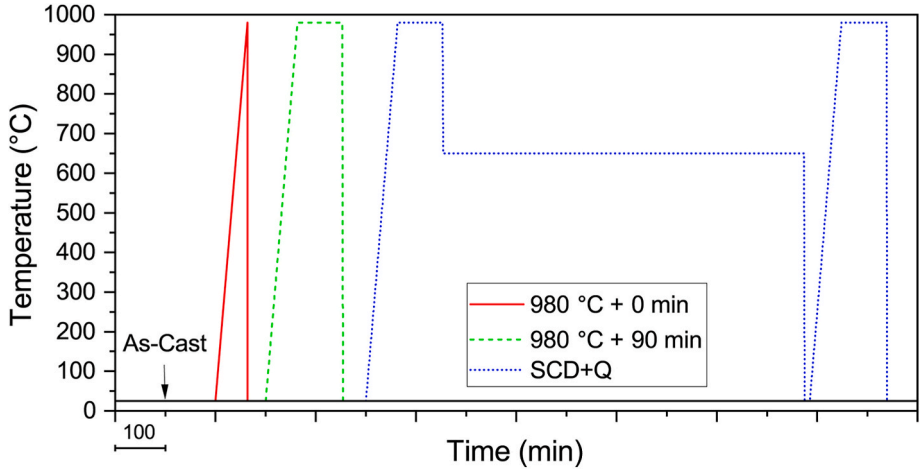

Fig. 1. Schematic of the four different heat treatments performed on the HCCI samples.

post processing of the images using the image analysis (I-A) software, ImageJ (version 1.52p) [27,28]. The micrographs were captured at a magnification of 2500×, covering an area of approximately 50 × 50 μm^2. In each case, 6 micrographs were analysed for statistical significance. Considering the magnification and resolution of image acquisition, all pixelated particles having a diameter less than 100 nm were excluded from the analysis.

Nanoindentation maps of 200 × 150 indents were performed on each sample using a FI-I04 Femto-Indenter (Oxford Instruments - FemtoTools AG, Switzerland) with a diamond Berkovich indenter on a FT-S20,000 sensor. Each indentation was performed using a continuous stiffness measurement (CSM) method in displacement control mode. The indentations were each performed in ~1 s with an oscillation frequency of 150 Hz and an amplitude that linearly increased from 0.5 to 2.5 nm with increasing depth. The total time for each indentation including repositioning was ~2.5 s. Each indentation was performed to a specified depth of 190 nm, so that a spacing of 2 μm between indentations could be used while still ensuring an indentation depth/spacing ratio of 10 [8]. This avoids any significant interaction between neighboring indents. Hardness (H) and reduced elastic modulus (E_r) were measured as a function of depth for each location, and representative values for each were taken by averaging values from depths >150 nm to minimize the influence of indentation size effects for hardness values and >100 nm for modulus values.

To extract phase-level properties and segment the large, multidimensional datasets that result from mechanical microscopy, both statistical and machine-learning clustering approaches are applied. A recent review of the various statistical and machine learning approaches to segmenting indentation data is available [8] The statistical deconvolution method of Ulm et al. [29] which fits a series of Gaussian peaks to a property distribution is first applied to the measured hardness and reduced modulus values separately. In some cases, an additional 'interphase' cluster was included to account for indentations located on phase boundaries and gave intermediate results. This allowed for more accurate fitting of the property distributions. Then a multidimensional clustering algorithm, *Gaussian Mixture,* [30] is applied to both hardness and reduced modulus together. This algorithm models the data as independent observations from a mixture of bivariate normal distributions. An expectation maximization algorithm finds the mean and covariance matrices for the normal distributions which best fit the overall property distributions. This method can segment clusters which strongly differing in size or areal fraction. However, some interphase clusters were also used for this method. Further, it is suitable for segmenting data where the fitting parameters are correlated. The resulting phase level properties from both segmentation methods are then presented on a 2D histogram plot and compared and discussed.

3. Results and discussion

3.1. Microstructural characterization

The microstructures of the as-cast and heat-treated samples are shown in the SEM and EBSD images of Fig. 2. The as-cast material consists of a network of $(Cr,Fe)_7C_3$ EC (~30 %) dispersed in a matrix of austenite dendrites (~55–60 %). The presence of a martensitic layer (~10–15 %) at the interface of the two major phases, formed during solidification as result of a local C and Cr depletion, can be identified in the EBSD phase map (Fig. 2A2) [19]. The microstructure of the heat-treated samples contains a primarily martensitic matrix (α'), finely precipitated SC ($M_{23}C_6$ type), the original (as-cast) EC (M_7C_3 type), and some retained austenite (RA). A reduction in the austenitic fraction is observed with increasing the holding time during heat treatment. As previously demonstrated [18,31], the SC precipitation begins at the regions next to the EC, where the thin layer of martensite act as a specific nucleation site due to reduced activation energy required for carbide nucleation, which is a consequence of the large lattice distortion and non-equilibrium defects.

Moreover, the size and carbide volume fraction (CVF) of SC increased when the samples were held for longer times at the destabilization temperature, as detailed in Figs. 3 and 4. The implementation of a multi-step HT led to the largest size and CVF of the SC. Fig. 3 shows the evolution of the SC and RA content as function of the heat treatment. The observed reduction of RA is a consequence of the increase of the SC precipitation, as described by Nayak et al. [18]. The redistribution of alloying elements during destabilization results in the precipitation of $M_{23}C_6$-type SC. Their increase in size and CVF decreases the alloy element content in the matrix, particularly the carbon content necessary for stabilizing austenite.

4. Mechanical properties

Fig. 5 presents the hardness (H) and reduced elastic modulus (E_r) maps from the HCCI alloys containing 26.6 wt% Cr, highlighting significant variations in the mechanical properties of the different constitutive phases as a function of heat treatment (Fig. 5). These show a strong correspondence to their electron microscopy counterparts in Fig. 2.

Progressing through the heat treatments, a clear evolution in both microstructure and mechanical properties is observed when moving from the As-cast to the SCD + Q states. In the As-cast condition, the retained austenite (RA) phase is distinctly visible as 'blue' (low hardness) regions in the hardness maps, while the extremely hard eutectic carbides (EC) appear in 'red.' These carbides are surrounded by a thin 'gold' layer, representing martensite.

In the second condition, following a short destabilization treatment (980 °C for 0 min), a significant reduction in Retained Austenite is evident, as indicated by the decreased fraction of 'blue' regions in the micrograph. Conversely, the martensite phase has notably increased, appearing as 'green' and 'gold' regions. The observed variations in martensite hardness across the map will be explored in a later discussion.

In the third condition, following an extended destabilization treatment (980 °C for 90 min), retained austenite is nearly absent, leaving a microstructure composed of Eutectic Carbides and Martensite. In the fourth condition, after destabilization and sub-critical diffusion steps, the microstructure and property distribution remain largely similar to those observed in the third condition.

5. Statistical analysis

Statistical deconvolution of the extensive indentation dataset allows for a quantitative evaluation of individual constitutive phase, or phase-level, properties. The histograms in Figs. 6 and 7 depict the hardness and reduced elastic modulus of each investigated specimen, employing uniform bin sizes of 0.1 GPa and 1 GPa, respectively. These histograms illustrate a multimodal phase peak distribution centered at different mean values, as summarized in Table 1.

Statistical deconvolution of the indentation dataset provides quantitative evaluation of mechanical properties of individual constitutive phases. Notably, the outcomes from deconvoluting H histograms for the as-cast sample in Fig. 6 revealed four constitutive phases, with their respective values detailed in Table 1. Nonetheless, the microstructural analysis indicates only three phases present, namely austenite (~55–60 %), martensite (~10–15 %), and EC (~30 %), as shown in Fig. 2 and reported by Nayak et al. [18]. H1 corresponds to austenite, whose values fall between 3.5 GPa and 5.5 GPa depending on the alloy elements content [32]. H4 is the value corresponding to M7C3 EC, whose value varies with the Cr/Fe ratio [32,33]. The H2 value is assigned to the martensitic phase, whose value might vary between 5 and 9 GPa depending on the carbon content [32,34,35]. Additionally, the H3 value for the as-cast sample falls between H2 and H4, which might be related to the EC/α' interfaces [32], as depicted in Fig. 8a. On the other hand,

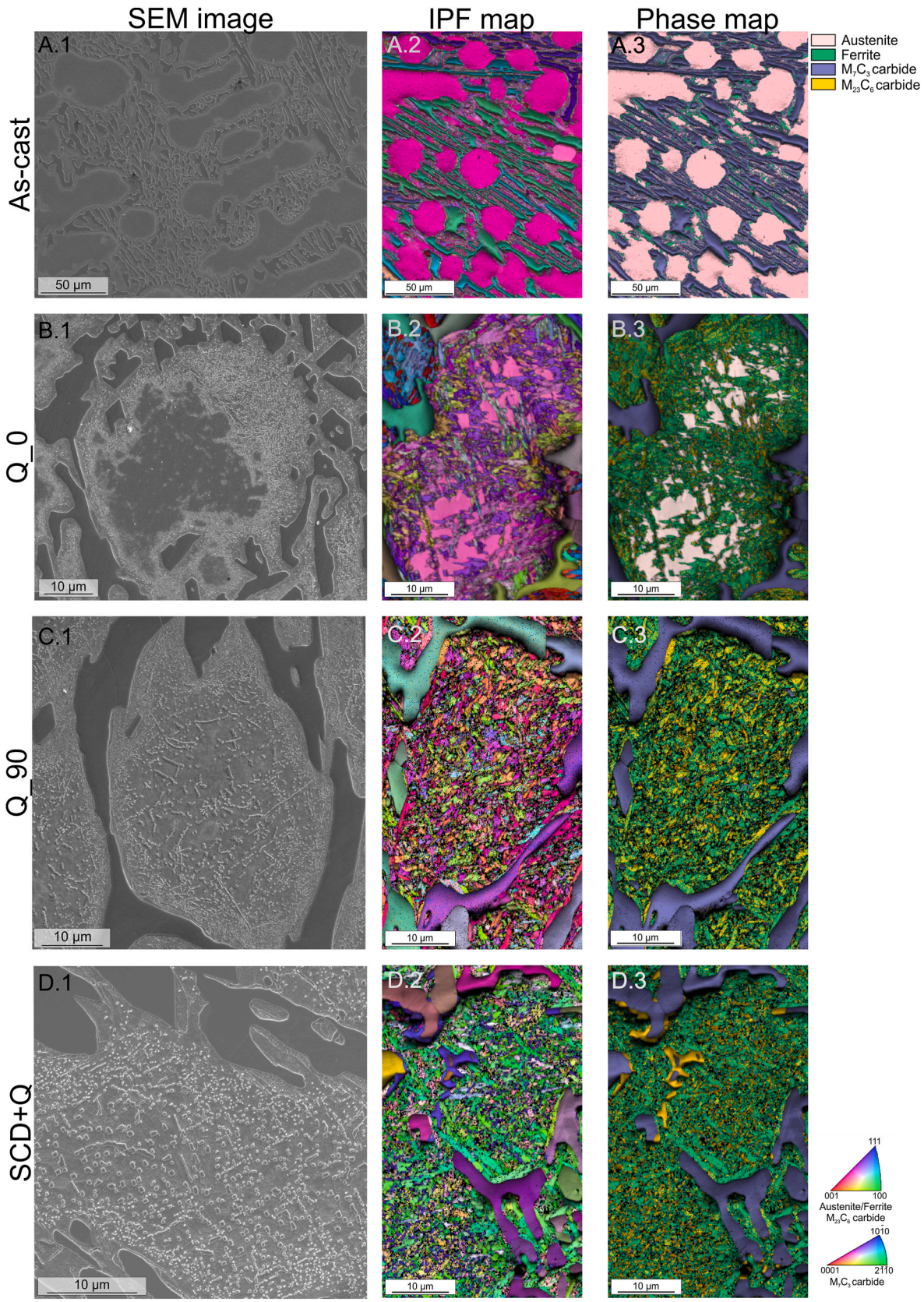

Fig. 2. Microstructural characterization of the as-cast and heat-treated samples. The figure shows the SEM images and EBSD phase and IPF maps. EBSD measurements in the as-cast condition were performed using a step size of 250 nm, whereas for the heat-treated samples 100 nm step size was employed. The SEM image does not correspond to the same area as the EBSD maps.

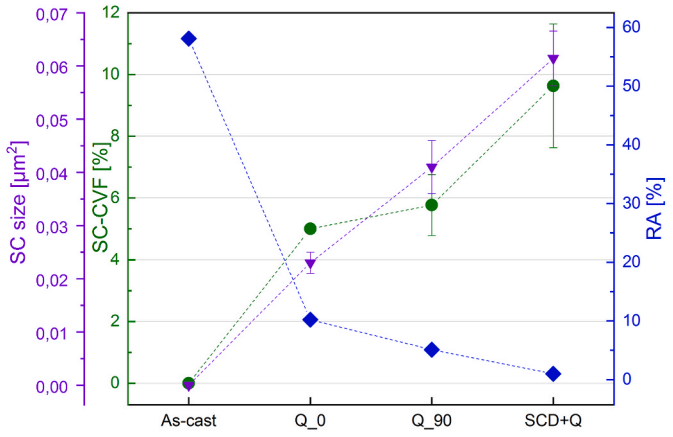

Fig. 3. The graph shows the fraction of RA (in blue) and of SC (in green) [18]. The RA fraction corresponding to the as-cast condition was metallographically determined as detailed in Ref. [23]. The RA value for the SCD + Q sample was estimated to be within the detection limit of the implemented methodology. (For interpretation of the references to color in this figure legend, the reader is referred to the Web version of this article.)

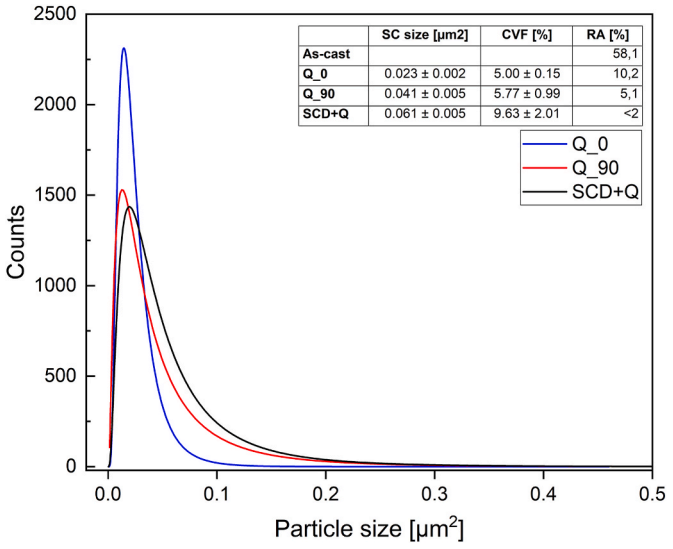

Fig. 4. Particle size distribution for the heat-treated samples. The tendency towards a larger particle size is observed from Q_0 to Q_90, and finally to SCD + Q. Quantification of the microstructural components corresponding to the different analysed samples [5,18]. SC size header on the inset table corresponds to the "average SC size".

the E-histogram displays three peaks that correspond with the values denoting austenite, martensite, and M7C3 EC. When evaluating the phase fractions obtained from deconvoluting the *E*-histrogram, the EC fraction is in accordance with the microstructure quantification [18,23]. The apparent fraction of austenite and martensite phases is influenced by the overlapping of the peaks in the distribution due to the interphases effect, as shown in Fig. 8a, where it is possible to see the frequency of indentations reaching the interfaces. The presence of a martensitic layer at the γ/EC interphase led to the creation of two other interfaces, γ/α' and α'/EC. In addition, since the martensite is formed during solidification due to chemical gradients, it is also expected a variation of the mechanical response, principally due to a variable carbon content within the martensite.

The Q_0 sample, exposes a more intricate microstructure, because of the SC precipitation from the destabilized austenite during heating to 980 °C. The microstructure consists of a significant fraction of RA and SC embedded into a martensitic matrix (Figs. 2 and 4). Thus, the chemical variations are accompanied by gradients in the mechanical properties, represented by the hardness shifts depicted in the *H*-histogram. This outcome stems from the pronounced microstructural inhomogeneity. The increase in the H value of the austenite (from ~4.2 to ~5.2 GPa) is attributed to solid solution hardening, resulting from the redistribution of alloying elements that concentrate in the RA. Two additional components are present in the H (Q_0)-histogram, corresponding to the interfaces between austenite/martensite and EC/martensite regions. The *E*-histogram exhibits three components, which correspond to austenite, EC, and martensite.

As shown in Fig. 2 and mentioned previously, finely dispersed $M_{23}C_6$ secondary carbides (~5 % fraction) can be found that are surrounded by a locally transformed martensite matrix. Due to the size of SC with respect to the indentation size, the probability of indenting a single SC particle is low, especially in the Q_0 sample, where the SC present an average equivalent diameter of approximately 150–170 nm (Fig. 2). Therefore, data extracted from *H*- and *E*-histograms (Figs. 6 and 7) reflect the composite mechanical response of the metallic matrix with SC reinforcement. The increased hardness observed in the martensitic matrix is attributed to precipitation strengthening from fine $M_{23}C_6$ carbides, which are likely to nucleate at defect-rich regions [18,31].

H distributions for the Q_90 sample show two peak values, H_1 and H_2, that are close to each other and that clearly represent the chemical gradients within the matrix. After 90 min destabilization at 980 °C there is a larger fraction of SC with larger size (Fig. 2), while RA fraction was reduced. Values for H_4 and H_3 correspond to the EC and EC/martensite interfaces, respectively.

The SCD + Q sample exhibits an average SC size that is 50 % larger than the Q_90, and these carbides are embedded in a martensitic matrix due to an extended holding time at the destabilization temperature. The increased size and CVF of SC contribute to higher H_1 and H_2 values, as a result of precipitation strengthening. Notably, a decline in hardness is observed in relation to the EC and the corresponding EC/matrix interfaces. Fig. 11 illustrates a transformation from M_7C_3 to $M_{23}C_6$ in the EC, attributed to carbon migration from carbides to the matrix. This $M_7C_3/M_{23}C_6$ in-situ transformation in the EC, with $M_{23}C_6$ forming the shell and M_7C_3 forming the core, aligns with findings reported in HCCI and high-carbon martensitic steels by several authors [38]. The transformation results in a distinctive core-shell structure, as depicted in Fig. 9.

6. Comparison and analysis

To obtain representative distributions of the investigated mechanical properties for each constitutive phase present in the microstructures of the HCCI alloys, 2D-histogram [39] graphs are presented in Fig. 10. The graphs simultaneously display *H* and E_r values, providing an insightful visual representation of the data. The data in the 2D histograms allows easy visual separation of the different phases present in the HCCI samples as a function of heat treatment. These representations include the *H* and E_r values obtained from 30 000 imprints conducted on each investigated specimen. In this type of graph, the color of each pixel/bin represents the number of indentations that are included within a range of *H* and E_r, which is defined as a 2D bin size. This highlights the peak locations or cluster centers corresponding to the mean values of *H* and E_r for the identified phases present on the region of interest and includes labels of the statistical peak and cluster locations with standard deviations from both statistical deconvolution and machine-learning clustering methods [29,36,37]. Individual phases are represented as clusters, while overlapping clouds highlight regions where two phases interact, resulting from indentations at phase boundaries that capture transitional mechanical properties.

Alongside these 2D histograms, H/E_r ratio maps overlaid on backscattered electron micrographs are presented (Fig. 9) to illustrate the relationship between property distributions and microstructure with

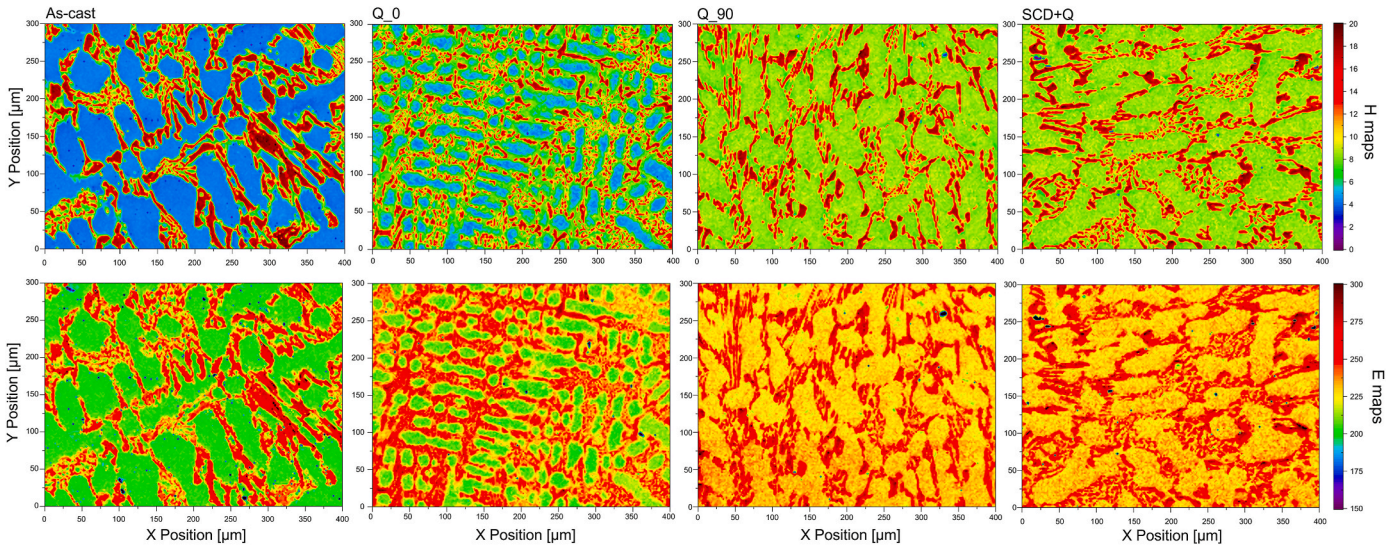

Fig. 5. Hardness (H) and reduced elastic modulus (E_r) maps obtained from nanoindentation measurements performed on HCCI alloy containing 26.6 wt% Cr in the as-cast state and after different thermal treatments (Q_0; Q_90 and SCD + Q). (For interpretation of the references to color in this figure legend, the reader is referred to the Web version of this article.)

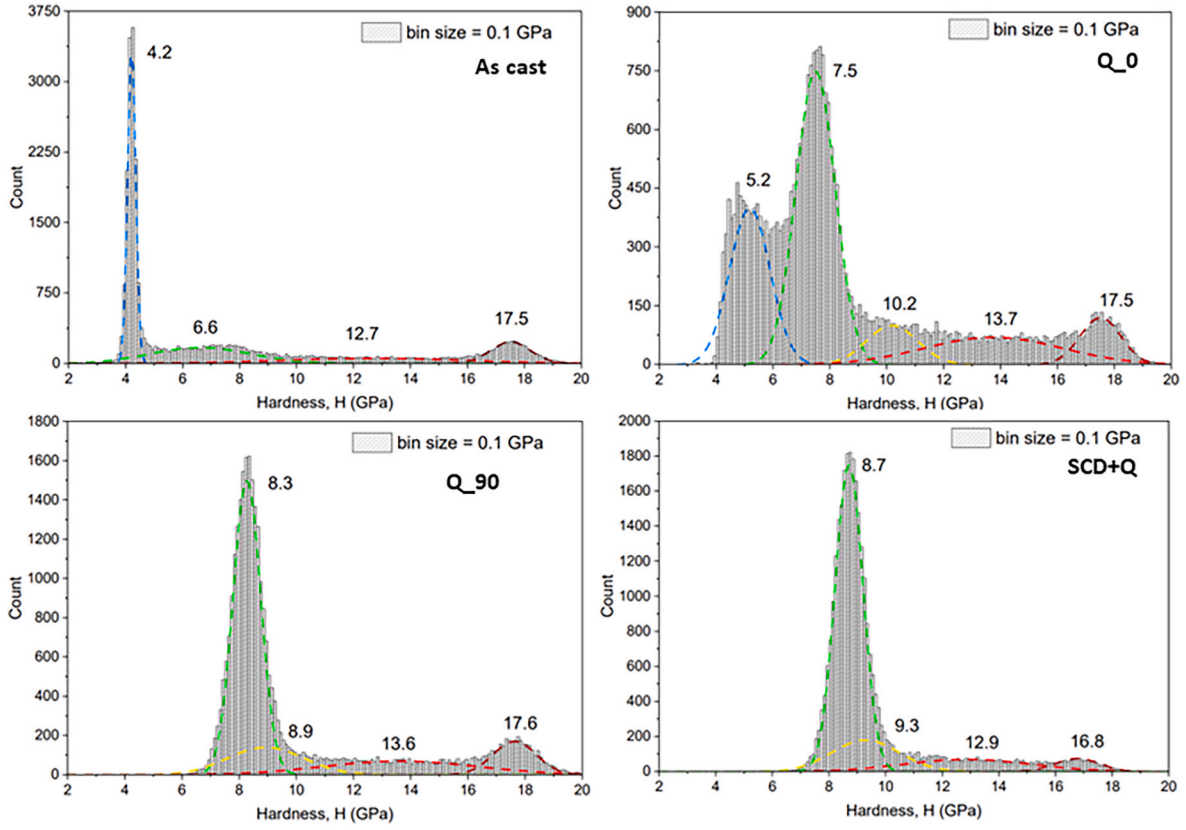

Fig. 6. Histogram of hardness values (bin size 0.1 GPa) determined from 30 000 indentations performed under displacement control mode at 190 nm of maximum penetration depth. The simulated hardness distribution function using the statistical fitting parameters (summarized in Table 1) are overlapped in the hardness histogram for the different investigated microstructures on HCCI alloy containing 26.6 wt% Cr. Note that the Y-axis scales vary, but the bin size is consistently maintained across all histograms.

heat treatment. Although H - and E_r -maps highlight different mechanical behavior for each constitutive phase, they are interrelated in such a way that the corresponding H/E_r ratio maps demonstrate more consistent values. This representation highlights differences related to the different constitutive phases present in the region of interest, particularly in terms of chemical composition. Since indentation hardness combines the measurement of reversible (elastic) and irreversible (plastic) deformation, the hardness maps are intrinsically convoluted with the elastic modulus maps. Representing H/E_r ratio provides a better description of the plasticity of the material, i.e. H/E_r describes the

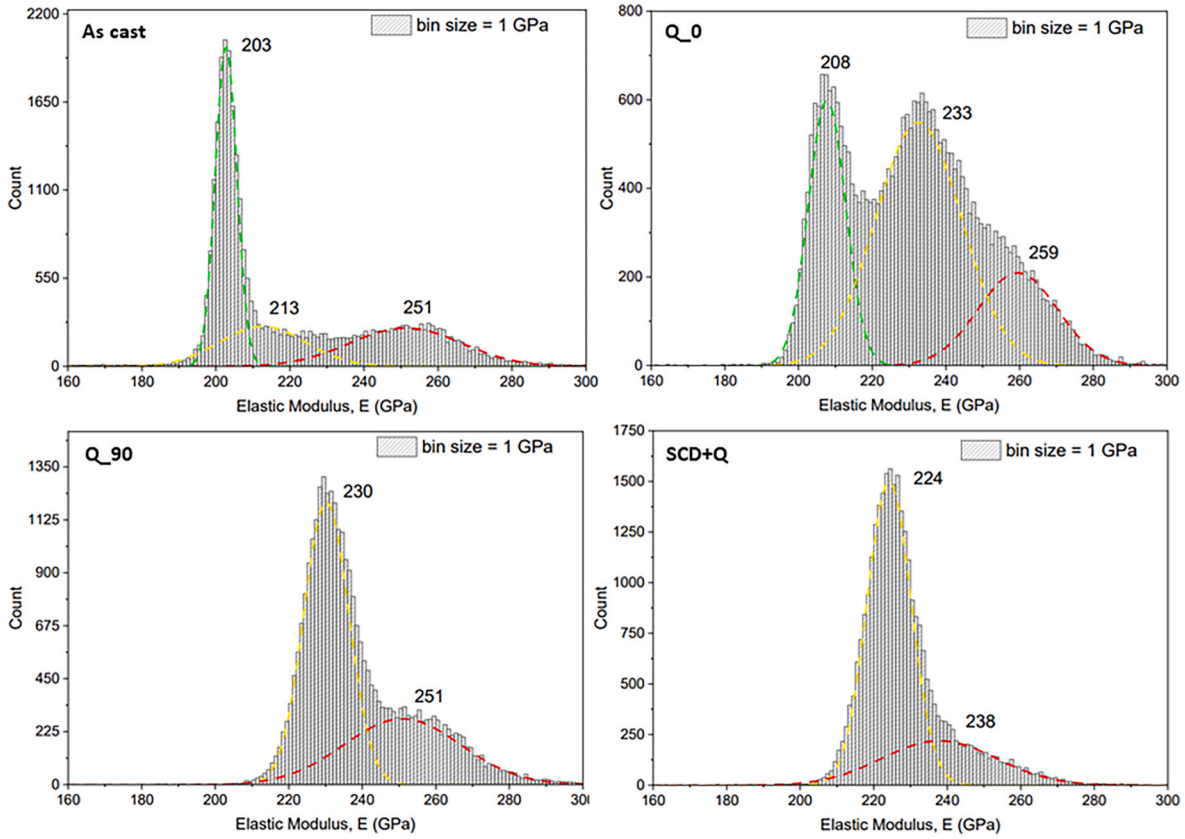

Fig. 7. Histogram of the reduced elastic modulus values (bin size 1 GPa) determined from 30 000 imprints performed under displacement control mode at 190 nm of maximum penetration depth. The simulated elastic modulus distribution function using the statistical fitting parameters (summarized in Table 1) are overlapped in the hardness histogram for the different investigated microstructures on HCCI alloy containing 26.6 wt% Cr. Note that the Y-axis scales vary, but the bin size is consistently maintained across all histograms.

Table 1
Summary of the H and E for each constitutive phase determined by using the Ulm and Constantinides Method [29,36,37] on 26.6 wt% Cr cast iron material (as-cast) and with different thermal treatments (Q_0; Q_90 and SCD + Q). The values for the H and E are in GPa. The f_i denotes the content of each constitutive phase on the region of study in %.

	As-cast	Q_0	Q_90	SCD + Q
H_1	4.2 ± 0.1 (austenite)	5.2 ± 0.7 (austenite)	8.3 ± 0.5 (martensite)	8.7 ± 0.5 (martensite)
H_2	6.6 ± 1.7 (martensite)	7.5 ± 0.7 (martensite)	8.9 ± 1.3	9.3 ± 1.2
H_3	12.7 ± 3.2 (EC + matrix interface)	10.2 ± 0.9	13.6 ± 2.7 (EC + matrix interface)	12.9 ± 2.2 (EC + matrix interface)
H_4	17.5 ± 0.7 (EC)	13.7 ± 2.41 (EC + matrix interface)	17.6 ± 0.7 (EC)	16.8 ± 0.8 (EC)
H_5	–	17.5 ± 0.7 (EC)	–	–
f_{1_H}	43.9	27.0	60.6	70.7
f_{2_H}	26.8	45.5	13.5	12.9
f_{3_H}	17.4	6.66	16.2	13.1
f_{4_H}	11.9	14.9	9.7	3.3
f_{5_H}	N/A	5.94	N/A	N/A
E_1	203 ± 3	208 ± 5	230 ± 6	224 ± 6
E_2	212 ± 12	233 ± 11	251 ± 16	238 ± 16
E_3	251 ± 15	259 ± 11	N/A	N/A
f_{1_E}	45.4	25.7	58.7	70.1
f_{2_E}	23.3	56.1	41.3	29.9
f_{3_E}	31.3	18.2	N/A	N/A
X^2_H (–)	$7.51{\cdot}10^{-6}$	$9.66{\cdot}10^{-6}$	$1.04{\cdot}10^{-6}$	$5.58{\cdot}10^{-7}$
X^2_E (–)	$4.35{\cdot}10^{-6}$	$2.12{\cdot}10^{-6}$	$1.82{\cdot}10^{-6}$	$1.41{\cdot}10^{-6}$
R^2_H (–)	0.99910	0.99988	0.99999	0.99999
R^2_E (–)	0.99995	0.99997	0.99998	0.99998

resistance of a material to irreversible deformation [26].

Particularly, for the as-cast, two clear peaks can be immediately identified in Fig. 10. They correspond to the two majoritarian phases; one located at H ~4 GPa and E_r ~200 GPa, corresponding to the austenitic matrix, and the other at H ~17.5 GPa/E ~255 GPa, corresponding to the M_7C_3 type EC. Also, for the as-cast specimen a non-majoritarian peak appears at H ~7 GPa and E_r ~210 GPa, that represents the martensitic phase observed at the γ/EC interface in the as-cast condition (Fig. 2a).

A similar trend can be appreciated for the Q_0, with the cluster at H

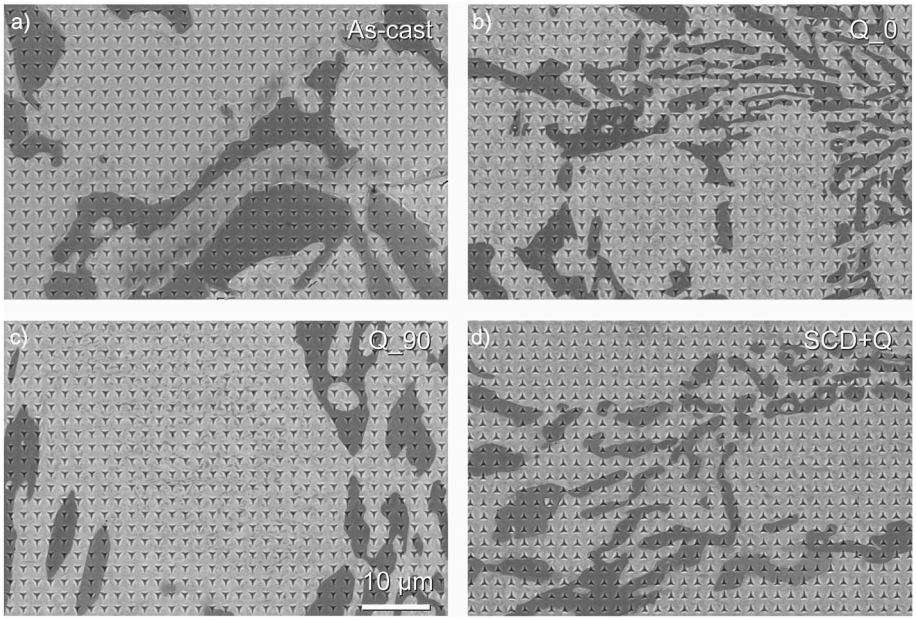

Fig. 8. a) as-cast sample showing the eutectic (EC/α') and austenitic regions where the imprints covering the EC/α' interfaces are clearly seen; b) Q_0 sample where the SC are barely identified due to their size; c) Q_90 sample showing the SC precipitated within the martensitic matrix; d) SCD + Q sample showing the nano-indentation imprints covering both the matrix and SC.

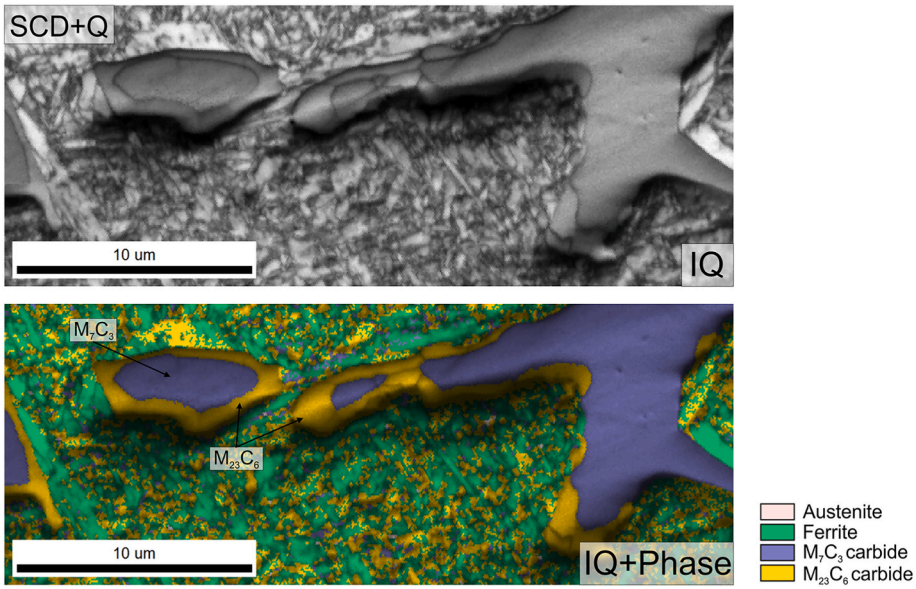

Fig. 9. EC undergoing a partial transformation from M_7C_3 to $M_{23}C_6$ due to prolonged exposure to elevated temperature during the HT cycle. (For interpretation of the references to color in this figure legend, the reader is referred to the Web version of this article.)

~7 GPa and E_r ~240 GPa showing a high density. Despite not being maintained at the destabilization temperature, the specimen shows discernible microstructural modifications (see Fig. 2b). There, M_7C_3 and $M_{23}C_6$ type SC precipitated in the regions close to the EC, depleting the matrix of C and Cr and allowing the partial γ to α'transformation during quenching [18,31]. The Q_0 sample shows, additionally to the cluster at H ~17.5 GPa/E_r ~255 GPa from the EC, two peaks at H ~5 GPa/E_r ~220 GPa and H ~7 GPa/E_r ~240 GPa, which might be correlated to the RA and the transformed region composed by martensite and SC that can be seen in the EBSD micrographs presented in Fig. 2. It is worth noting the diffusion and phase transformation processes occurring in this condition. As demonstrated by Guitar et al. [31], SC precipitation starts at the austenite/EC interface, a martensitic region depleted of alloy elements. Since the material had not sufficient time at the destabilization temperature, the alloy elements cannot be homogeneously distributed within the matrix. Martensite containing variable concentrations of alloy elements forms during cooling. Consequently, gradients in the chemical composition translate in gradients in the mechanical properties of the material.

On the other hand, Q_90 and SCD + Q samples present a similar behavior, showing two different peaks, which corresponds to the two majoritarian phases identified by EBSD in Fig. 2; one located at H ~8 GPa and E_r ~225–230 GPa and the other located at H ~18 GPa and E_r ~250 GPa, corresponding to the Martensite + SC and EC, respectively. Furthermore, the tail of pixels below the main peaks corresponds to minoritarian phases with a size smaller than the plastic and elastic field

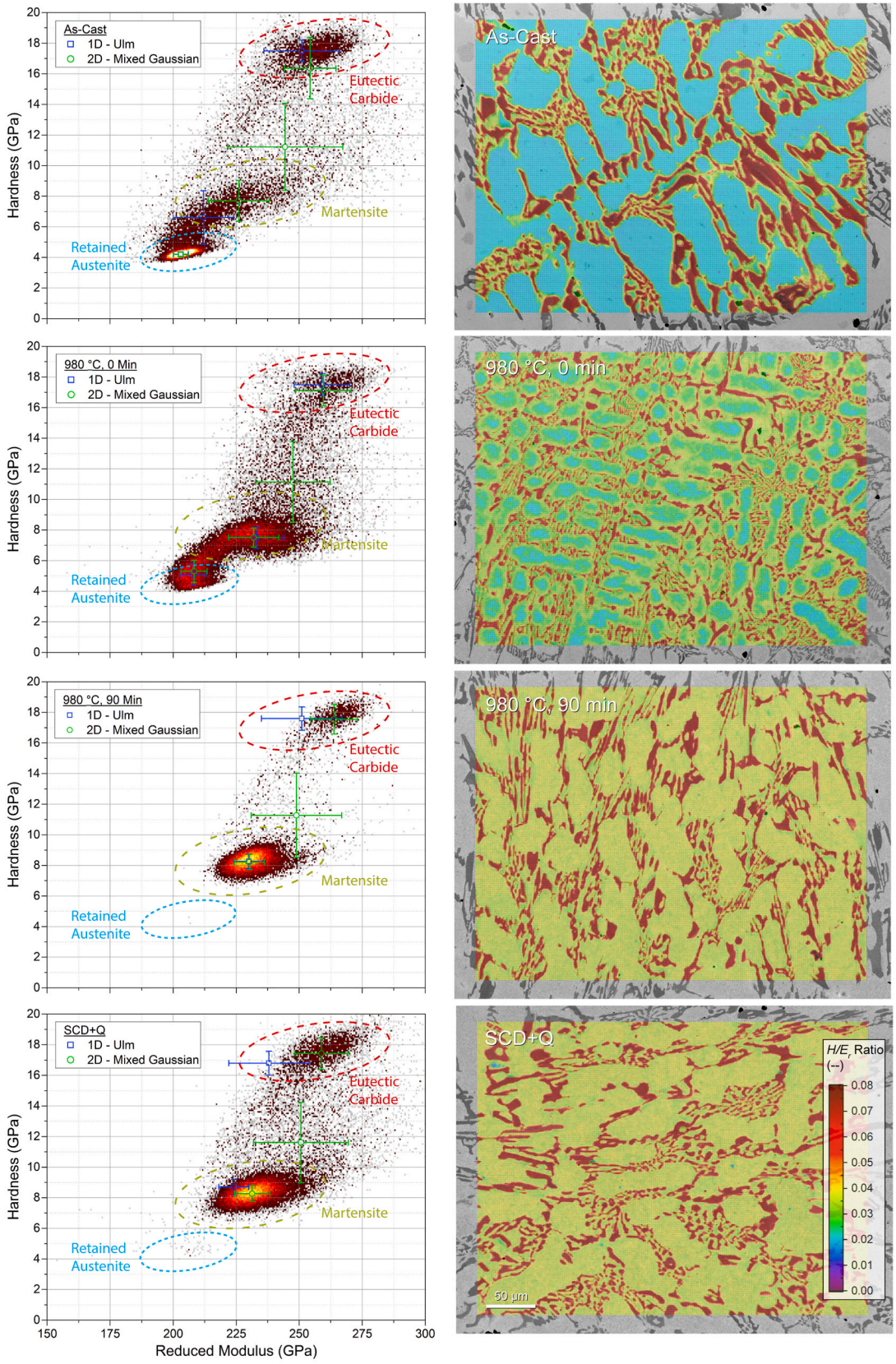

Fig. 10. 2D histograms and H/E_r ratio maps overlaid on back-scattered electron (BSE) micrographs showing the evolution of the microstructures and their properties as a function of heat treatment with the phase regions labeled and statistical/cluster locations and standard deviations. (For interpretation of the references to color in this figure legend, the reader is referred to the Web version of this article.)

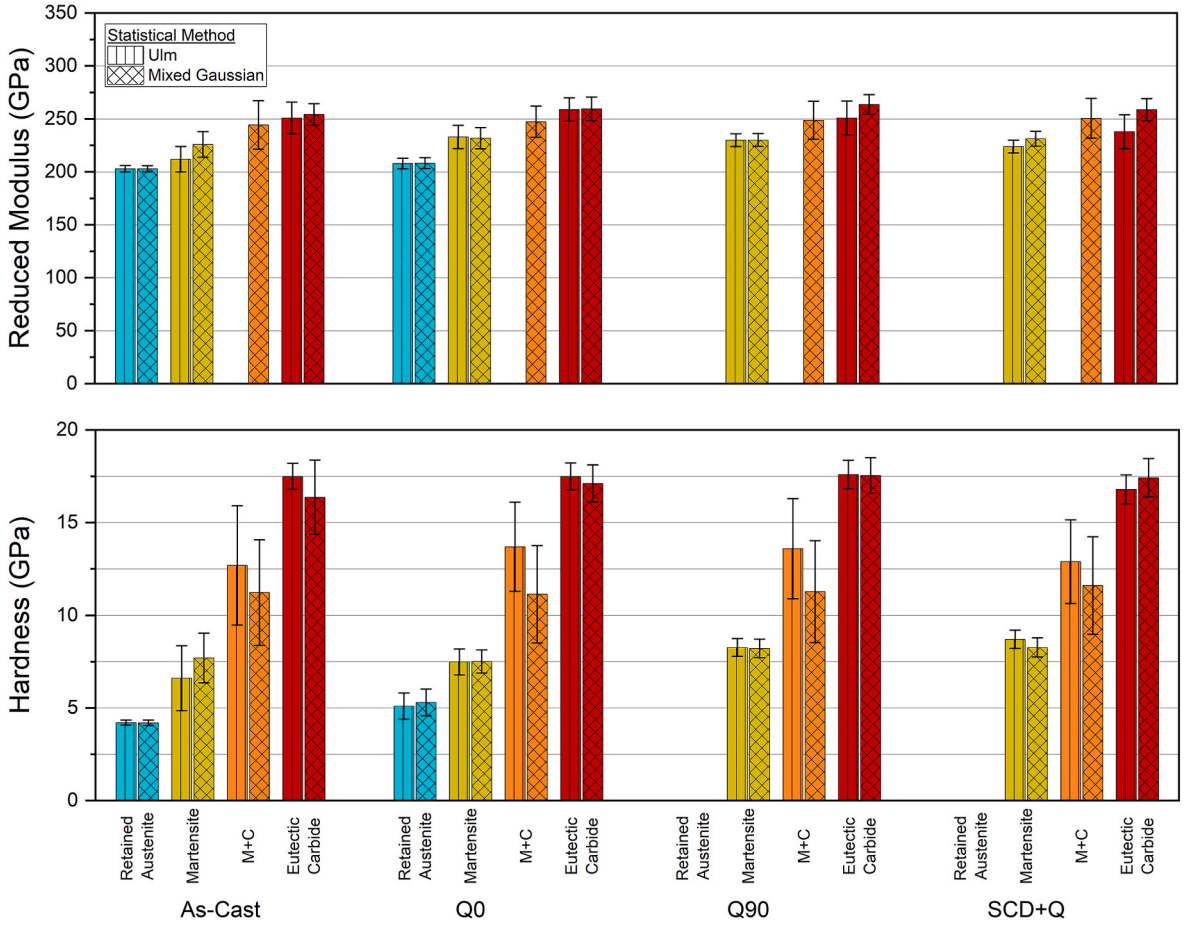

Fig. 11. Phase-level properties as a function of heat treatment and data segmentation method.

induced during the indentation process. Intensity values between the peaks or clusters correspond to indentations conducted at the phase boundaries and whose plastic zones included two phases, therefore having a composite-like response.

Statistical property extraction allows the separation of the individual phases for the determination of the fraction, average value, and variation of each constitutive phase [13,40]. However, the strong variation in the mechanical properties and the finely-mixed microstructure, especially in the heat-treated state, represent a challenge in the assigning the properties values to the corresponding constitutive phase.

Fig. 11 shows a more conventional approach to presenting the deconvoluted/clustered data shown overlaid on the 2D histograms from Fig. 10. The phase-level properties of each phase, as determined by the two methods, are shown for each heat treatment. As can be seen in Fig. 11, the two methods are generally in good agreement. The only significant discrepancies are observed in the last two heat treatments for the Eutectic Carbide phase, where the one-dimensional method underestimates the reduced modulus of the cluster. This substantial agreement between the two methods validates the performance of the unsupervised, Mixed Gaussian clustering algorithm in comparison to the more labor-intensive statistical deconvolution method.

High-speed nanoindentation (NI) mapping and statistical/clustering deconvolution are useful tools for evaluating the multiphase microstructure of the HCCI alloy, particularly in both the as-cast and heat-treated states. This approach facilitates the identification of correlations between microstructure and mechanical properties. This is particularly evident in the reduction of hardness of the EC associated with the transformation from M_7C_3 to $M_{23}C_6$. The application of elastic modulus histograms offers a precise depiction of the mechanical response of individual microstructural components in HCCI after undergoing various microstructural modifications. Both the as-cast and Q_0 samples display *E*-histograms with three distinct peaks that correspond to the primary microstructural constituents: austenite, martensite, and M_7C_3 type EC. Although the Q_0 sample contains SC, their average size is 150–170 nm (equivalent diameter). This statement suggests that they act as a reinforcement to the martensitic phase rather than as a standalone component.

Although direct tribological testing was not performed in this study, previous research carried out by Nayak et al. [18] has shown that differences in phase distribution and mechanical properties significantly influence wear behavior in these alloys. In particular, the Q_0 condition exhibited improved wear resistance, despite Q_90 and SCD + Q possessing higher matrix hardness. This suggests that the dual-phase nature of Q_0, with austenite and martensite coexisting, may enhance load distribution and accommodate deformation, providing additional support to surrounding carbides.

The nanoindentation results presented in this work further support this interpretation. As shown in Fig. 10, Q_0 exhibits a broader distribution in hardness (H) and reduced elastic modulus (E) values compared to Q_90 and SCD + Q. This heterogeneous mechanical response suggests a mixed-phase matrix capable of locally adjusting to mechanical stresses, which may help prevent brittle fracture of the eutectic carbides (EC) during wear. The H/Er ratio maps in Fig. 10 further reinforce this behavior, as Q_0 displays a dual clustering effect, indicating regions with distinct elastic-to-plastic deformation characteristics. This mechanical duality likely enables the retained austenite to deform plastically under stress, redistributing loads and preventing premature carbide fracture, factors that have been shown to improve wear resistance in high-chromium cast irons [41].

The nanoindentation-based phase mapping highlights how

differences in local mechanical properties, particularly in Q_0, may contribute to superior wear resistance by balancing hardness and compliance in an optimized microstructural configuration. The insights gained through high-speed nanoindentation mapping in this study provide a powerful framework for understanding how microstructural evolution influences material performance beyond simple hardness metrics. In contrast, Q_90 and SCD + Q exhibit a more uniform and harder matrix, as indicated by their tighter mechanical clustering in H-E space. While this enhances overall hardness, it also reduces matrix compliance, making the material less capable of accommodating local deformation. This could explain why these conditions exhibited increased carbide cracking and spallation during wear testing in prior studies. The increased stiffness of the martensitic matrix in these samples likely limits their ability to redistribute stresses, resulting in localized stress concentration at carbide-matrix interfaces, which can accelerate material loss during wear. It is important to note that for evaluating the wear resistance of a multicomponent material, as is the case of HCCI, the hardness should not be the only factor to consider, but also phase interactions, mechanical gradients, and local compliance variations within the matrix.

7. Conclusions

The influence of the applied heat-treatments on HCCI alloys was investigated in terms of microstructural evolution and mechanical integrity at the sub-micrometric length scale using analytical electron microscopy, and high-speed nanoindentation mapping. Four different heat treatment conditions were investigated. Four distinct sample conditions were the subject of investigation. The proportion of austenitic phase in the samples subjected to analysis exhibited a range from approximately 60 % to less than 2 %. The quantity and dimensions of the SC in the heat-treated samples exhibited a variation of 5–10 % and equivalent diameters of 150–300 nm, respectively.

To track the statistical properties of the main phases across different heat treatments, two approaches were applied: a conventional statistical deconvolution method (Ulm's method) and a machine-learning-based Mixed Gaussian clustering approach. Both methods yielded consistent hardness and reduced modulus values for the primary phases, confirming the robustness of the clustering approach. Based on the results presented in this study, the following conclusions can be drawn.

(1) 2D histograms provide a more detailed and accurate representation of the mechanical response of individual microstructural components within HCCI, effectively capturing the influence of microstructural modifications due to heat treatment.
(2) Due to their nanometric size and distribution, SC do not behave mechanically as independent phases but rather act as reinforcing elements within the matrix, leading to an increment in hardness and elastic modulus of the RA and martensitic phase.
(3) 2D histograms of hardness versus elastic modulus serve as an effective visualization tool for interpreting the mechanical behavior of multiphase materials, demonstrating a strong correlation between mechanical property mapping and resultant microstructure.
(4) High-speed nanoindentation mapping combined with advanced statistical and machine learning analysis proves to be an effective method for characterizing the phase-level mechanical performance of HCCI alloys across different heat treatments conditions.

CRediT authorship contribution statement

M.A. Guitar: Writing – original draft, Formal analysis, Conceptualization. **U.P. Nayak:** Writing – review & editing, Methodology, Conceptualization. **G. Riu-Perdrix:** Investigation, Data curation. **J.M. Wheeler:** Writing – review & editing, Methodology, Formal analysis. **J. J. Roa:** Writing – review & editing, Methodology, Formal analysis.

Declaration of competing interest

The authors declare that they have no known competing financial interests or personal relationships that could have appeared to influence the work reported in this paper.

Acknowledgements

The present work is supported by funding from the Deutsche Forschungsgemeinschaft (DFG, project: GU 2102/2-1). The authors would like to thank Martin Duarte from Tubacero S.A. for providing the materials. The authors would like to acknowledge the financial support of the Mat-Innovat (Kreislauffähige Materialsysteme für innovative Hochleistungswerkstoffe") project supported by the State of Saarland from the European Regional Development Fund (Europäischer Fond für Regionale Entwicklung, EFRE). Open Access funding enabled and organized by Project DEAL.

Appendix A. Supplementary data

Supplementary data to this article can be found online at https://doi.org/10.1016/j.msea.2025.148461.

Data availability

Data will be made available on request.

References

[1] G.L.F. Powell, R.A. Carlson, V. Randle, The morphology and microtexture of M7C3carbides in Fe-Cr-C and Fe-Cr-C-Si alloys of near eutectic composition, J. Mater. Sci. 29 (1994) 4889–4896, https://doi.org/10.1007/BF00356539.
[2] S.D. Carpenter, D. Carpenter, J.T.H. Pearce, XRD and electron microscope study of an As-Cast 26 . 6 % chromium white iron microstructure, Mater. Chem. Phys. 85 (2004) 32–40, https://doi.org/10.1016/j.matchemphys.2003.11.037.
[3] S.D. Carpenter, D.E.O.S. Carpenter, J.T.H. Pearce, The nature of stacking faults within iron-chromium carbide of the type (Fe,Cr)7C3, J. Alloys Compd. 494 (2010) 245–251, https://doi.org/10.1016/j.jallcom.2009.12.197.
[4] S.D. Carpenter, D. Carpenter, J.T.H. Pearce, XRD and electron microscope study of a heat treated 26.6% chromium white iron microstructure, Mater. Chem. Phys. 101 (2007) 49–55, https://doi.org/10.1016/j.matchemphys.2006.02.013.
[5] M.A. Guitar, U.P. Nayak, D. Britz, F. Mücklich, The effect of thermal processing and chemical composition on secondary carbide precipitation and hardness in high-chromium cast irons, Int. J. Metalcast. 14 (2020) 755–765, https://doi.org/10.1007/s40962-020-00407-4.
[6] M.A. Guitar, A. Scheid, S. Suárez, D. Britz, M.D. Guigou, F. Mücklich, Secondary carbides in high chromium cast irons: an alternative approach to their morphological and spatial distribution characterization, Mater. Char. 144 (2018) 621–630, https://doi.org/10.1016/j.matchar.2018.08.020.
[7] M.A. Guitar, S. Suárez, O. Prat, M. Duarte Guigou, V. Gari, G. Pereira, F. Mücklich, High chromium cast irons: destabilized-subcritical secondary carbide precipitation and its effect on hardness and wear properties, J. Mater. Eng. Perform. 27 (2018) 3877–3885, https://doi.org/10.1007/s11665-018-3347-1.
[8] E. Rossi, J.M. Wheeler, M. Sebastiani, High-speed nanoindentation mapping: a review of recent advances and applications, Curr. Opin. Solid State Mater. Sci. 27 (2023).
[9] J.J. Roa, G. Fargas, A. Mateo, E. Jiménez-Piqué, Dependence of nanoindentation hardness with crystallographic orientation of austenite grains in metastable stainless steels, Mater. Sci. Eng., A 645 (2015) 188–195, https://doi.org/10.1016/j.msea.2015.07.096.
[10] J.J. Roa, E. Jimenez-Pique, C. Verge, J.M. Tarragó, A. Mateo, J. Fair, L. Llanes, Intrinsic hardness of constitutive phases in WC-Co composites: nanoindentation testing, statistical analysis, WC crystal orientation effects and flow stress for the constrained metallic binder, J. Eur. Ceram. Soc. 35 (2015) 3419–3425, https://doi.org/10.1016/j.jeurceramsoc.2015.04.021.
[11] J.J. Roa, E. Jiménez-Piqué, J.M. Tarragó, D.A. Sandoval, A. Mateo, J. Fair, L. Llanes, Hall-petch strengthening of the constrained metallic binder in WC–Co cemented carbides: experimental assessment by means of massive nanoindentation and statistical analysis, Mater. Sci. Eng., A 676 (2016) 487–491, https://doi.org/10.1016/j.msea.2016.09.020.
[12] J.J. Roa, P. Sudharshan Phani, W.C. Oliver, L. Llanes, Mapping of mechanical properties at microstructural length scale in WC-Co cemented carbides: assessment of hardness and elastic modulus by means of high speed massive nanoindentation and statistical analysis, Int. J. Refract. Metals Hard Mater. 75 (2018) 211–217, https://doi.org/10.1016/j.ijrmhm.2018.04.019.
[13] H. Besharatloo, S. Gordon, T. Rodriguez-Suarez, A. Can, W.C. Oliver, L. Llanes, J. J. Roa, Small-scale mechanical properties of constitutive phases within a

polycrystalline cubic boron nitride composite, J. Eur. Ceram. Soc. 39 (2019) 5181–5189, https://doi.org/10.1016/j.jeurceramsoc.2019.08.023.
[14] S. Gordon, H. Besharatloo, J. Wheeler, T. Rodriguez-Suarez, J. Roa, E. Jiménez-Piqué, L. Llanes, Micromechanical mapping of polycrystalline cubic boron nitride composites by means of high-speed nanoindentation: assessment of microstructural assemblage effects, J. Eur. Ceram. Soc. 43 (2023) 2968–2975, https://doi.org/10.3929/ethz-b-000601528.
[15] Y.T. Cheng, Z. Li, C.M. Cheng, Scaling relationships for indentation measurements, Philos. Mag. A 82 (2002) 1821–1829, https://doi.org/10.1080/01418610208235693.
[16] B.D. Beake, The influence of the H/E ratio on wear resistance of coating systems – insights from small-scale testing, Surf. Coat. Technol. 442 (2022) 128272, https://doi.org/10.1016/J.SURFCOAT.2022.128272.
[17] U.P. Nayak, F. Mücklich, M.A. Guitar, Interplay between the microstructure and tribological performance of a destabilized 26 wt% Cr HCCI: the influence of temperature and heating rate, Tribol. Int. 185 (2023) 108532, https://doi.org/10.1016/j.triboint.2023.108532.
[18] U.P. Nayak, F. Mücklich, M.A. Guitar, Time - Dependant microstructural evolution and tribological behaviour of a 26 Wt % Cr white cast iron subjected to a destabilization heat treatment, Met. Mater. Int. (2022), https://doi.org/10.1007/s12540-022-01276-8.
[19] A. Bedolla-Jacuinde, L. Arias, B. Hernández, Kinetics of secondary carbides precipitation in a Hiqh-Chromium white iron, J. Mater. Eng. Perform. 12 (2003) 371–382, https://doi.org/10.1361/105994903770342881.
[20] Kh Abdel-Aziz, M. El-Shennawy, A.A. Omar, Microstructural characteristics and mechanical properties of heat treated High-Cr white cast iron alloys, Int. J. Appl. Eng. Res. 12 (2017) 4675–4686.
[21] U.P. Nayak, S. Suárez, V. Pesnel, F. Mücklich, M.A. Guitar, Load Dependent Microstructural Evolution in an As-Cast 26 % Cr High Chromium Cast Iron During Unlubricated Sliding, 2021.
[22] J.M. Wheeler, B. Gan, R. Spolenak, Combinatorial investigation of the Ni–Ta system via correlated high-speed nanoindentation and EDX mapping, Small Methods 6 (2022), https://doi.org/10.1002/smtd.202101084.
[23] U.P. Nayak, M.A. Guitar, F. Mücklich, A comparative study on the influence of chromium on the phase fraction and elemental distribution in As-Cast high chromium cast irons: simulation vs. experimentation, Metals (Basel) 10 (2020), https://doi.org/10.3390/met10010030.
[24] U. Pranav Nayak, M.A. Guitar, F. Mücklich, Evaluation of etching process parameter optimization in the objective specific microstructural characterization of As-Cast and heat treated HCCI alloy, Prakt. Metallogr. Pract. Metallogr. 57 (2020) 688–713, https://doi.org/10.3139/147.110682.
[25] H.M. Rietveld, A profile refinement method for nuclear and magnetic structures, J. Appl. Crystallogr. 2 (1969) 65–71, https://doi.org/10.1107/s0021889869006558.
[26] L. Lutterotti, Total pattern fitting for the combined size-strain-stress-texture determination in thin film diffraction, Nucl. Instrum. Methods Phys. Res. B 268 (2010) 334–340, https://doi.org/10.1016/j.nimb.2009.09.053.
[27] Johannes Schindelin, E.F. Ignacio Arganda-Carreras, V. Kaynig, M. Longair, T. Pietzsch, S. Preibisch, C. Rueden, S. Saalfeld, B. Schmid, J.-Y. Tinevez, et al., Fiji: an open-source platform for biological-image analysis, Nat. Methods 9 (2012) 676–682, https://doi.org/10.1038/nmeth.2019.
[28] U.P. Nayak, M. Müller, D. Britz, M.A. Guitar, F. Mücklich, Image processing using open source tools and their implementation in the analysis of complex microstructures, Pract. Metallogr. 58 (2021) 484–506, https://doi.org/10.1515/pm-2021-0039.
[29] F.J. Ulm, M. Vandamme, C. Bobko, J. Alberto Ortega, K. Tai, C. Ortiz, Statistical indentation techniques for hydrated nanocomposites: concrete, bone, and shale, J. Am. Ceram. Soc. 90 (2007) 2677–2692, https://doi.org/10.1111/j.1551-2916.2007.02012.x.
[30] Trevor Hastie, Robert Tibshirani, Jerome Friedman the Elements of Statistical Learning: Data Mining, Inference, and Prediction, 2001, 978-0-387-84858-7.
[31] M.A. Guitar, U.P. Nayak, L.C. Schneider, J. Schmauch, F. Mücklich, Analysis of the carbide precipitation and microstructural evolution in HCCI as a function of the heating rate and destabilization temperature, Sci. Rep. (2023) 1–11, https://doi.org/10.1038/s41598-023-36364-1.
[32] L. Chen, S. Iyengar, J. Zhou, K. Turba, J.E. Ståhl, Characterization of microstructure and mechanical properties of high chromium cast irons using SEM and nanoindentation, J. Mater. Eng. Perform. 24 (2015) 98–105, https://doi.org/10.1007/s11665-014-1245-8.
[33] S. Ma, J. Xing, Y. He, Y. Li, Z. Huang, G. Liu, Q. Geng, Microstructure and crystallography of M7</Inf>C3</Inf> carbide in chromium cast iron, Mater. Chem. Phys. 161 (2015) 65–73, https://doi.org/10.1016/j.matchemphys.2015.05.008.
[34] T. Ohmura, K. Tsuzaki, S. Matsuoka, Nanohardness measurement of high-purity Fe ±C martensite, Scr. Mater. 45 (2001).
[35] F. Zhang, A. Ruimi, D.P. Field, Phase identification of dual-phase (DP980) steels by electron backscatter diffraction and nanoindentation techniques, Microsc. Microanal. 22 (2016) 99–107, https://doi.org/10.1017/S1431927615015779.
[36] G. Constantinides, F.-J. Ulm, K. Van Vliet, On the use of nanoindentation for cementitious materials, Mater. Struct. 36 (2003) 191–196.
[37] G. Constantinides, K.S. Ravi Chandran, F.J. Ulm, K.J. Van Vliet, Grid indentation analysis of composite microstructure and mechanics: principles and validation, Mater. Sci. Eng., A 430 (2006) 189–202, https://doi.org/10.1016/j.msea.2006.05.125.
[38] A. Wiengmoon, T. Chairuangsri, J.T.H. Pearce, A microstructural study of destabilised 30wt %Cr-2.3wt %C high chromium cast iron, ISIJ Int. 44 (2004) 396–403, https://doi.org/10.2355/isijinternational.44.396.
[39] Y. Xiao, H. Besharatloo, B. Gan, X. Maeder, R. Spolenak, J.M. Wheeler, Combinatorial investigation of Al–Cu intermetallics using small-scale mechanical testing, J. Alloys Compd. 822 (2020), https://doi.org/10.1016/j.jallcom.2019.153536.
[40] H. Besharatloo, M. de Nicolás, J.J. Roa, M. Dios, A. Mateo, B. Ferrari, E. Gordo, L. Llanes, Assessment of mechanical properties at microstructural length scale of Ti(C,N)–FeNi ceramic-metal composites by means of massive nanoindentation and statistical analysis, Ceram. Int. 45 (2019) 20202–20210, https://doi.org/10.1016/j.ceramint.2019.06.292.
[41] U. Pranav, N. Saarbrücken, Interplay Between the Microstructure and Tribological Performance in Heat-Treated High Chromium Cast Iron Alloys, Saarland University, 2023.